ASME Journal of Mechanisms and Robotics
Online journal at:
https://asmedigitalcollection.asme.org/mechanismsrobotics

Yi Jin
Department of Mechanical and Aerospace Engineering,
The Ohio State University,
Columbus, OH 43210
e-mail: jin.1170@osu.edu

Hai-Jun Su[1]
Professor
Department of Mechanical and Aerospace Engineering,
The Ohio State University,
Columbus, OH 43210
e-mail: su.298@osu.edu

A Compliant Hinge Joint Driven by the PneuNets Bending Actuator

While soft robots enjoy the benefits of high adaptability and safety, their inherent flexibility makes them suffer from low load-carrying capacity and motion precision, which limits their applications to a broader range of fields. To address this problem, we propose a novel compliant hinge joint with a stiff backbone for load-carrying coupled with soft pneumatic networks (PneuNets) bending actuators. We derive a pseudo-rigid-body model of the joint design and validate it through experiments and simulations. The results show that the joint can achieve a large range of bending angles. The off-axis stiffness is from 16.74 to 627.63 times the in-axis stiffness. This design can carry a heavy load off-axis while maintaining the in-axis flexibility. This work lays out the foundation for designing high-performance soft robots by combining various flexure mechanisms and pneumatic bending actuators. [DOI: 10.1115/1.4064282]

Keywords: soft robots, compliant mechanism, pneumatic actuators, mechanism design, theoretical and computational kinematics

1 Introduction

Soft pneumatic robots have attracted much attention recently due to their safety, high adaptability, fast response, lightweight, and strong anti-interference ability [1]. As a result, a variety of soft pneumatic robots with different functions, such as climbing robots [2,3], walking robots [4,5], soft grippers [6,7], and soft pneumatic gloves [8,9], have been developed and applied in space exploration [10,11], medical field [12,13], and industrial field [14,15]. However, the inherent flexibility of soft pneumatic robots presents difficulties in carrying heavy loads and making precise motions, which restricts their further development.

Researchers propose two solutions to overcome this shortcoming. The first commonly used solution is the variable stiffness technique, which enables the soft robot to change stiffness through variable stiffness mechanisms or materials. For example, Kim et al. proposed a layer jamming mechanism, which uses negative pressure to change the friction between layers to achieve stiffness tuning [16]. Based on this work, Crowley et al. developed a positive layer jamming method to vary the stiffness of a soft pneumatic gripper [7]. Since the positive pressure has no upper limit, the positive layer jamming mechanism can change the stiffness in a more extensive range. In addition, some researchers have studied the inherent variable properties of smart materials for variable stiffness. Alambeigi et al. developed a continuum manipulator with a backbone made of phase-changing alloy [17], which changes the material's stiffness by controlling the temperature. Yang et al. designed a robotic finger that can control stiffness using shape-memory polymer joints [18]. Although the variable stiffness technique can overcome the challenges by tuning the stiffness, additional devices and space are required, increasing the cost and complexity of robots [19].

Another solution is a hybrid robot system combining stiff backbone mechanisms with soft joints. An example is a terrain-capable hybrid soft/stiff myriapod robot designed by Ozkan-Aydin et al. [20]. The soft joint of the robot enables it to adapt to the complex terrain well, and the rigid-body mechanism supports the robot's weight. However, rigid-body parts in this solution reduce the flexibility of the robots. Also, the robotic is hard to achieve high motion precision due to the compliance of the pure soft joint. Another example is a hybrid finger proposed by Lotifani et al. [21]. A rigid skeleton is embedded into a pneumatic soft finger to improve its torsional stiffness so that the gripper made of such fingers can grasp heavy objects. However, since the lateral bending stiffness has not been increased, it will still be unable to carry heavy objects and fail when the finger is extended to a certain length.

To improve this solution, we create a new hinge joint by combining compliant mechanisms (CM) [22] and PneuNets bending actuators. A typical compliant mechanism consists of a fixed and rigid moving stage. The two stages are connected by one or more flexure members. Compliant mechanisms offer many advantages over conventional rigid-body mechanisms, such as part-count reduction and reduced motion errors [22]. In addition, some CMs also have relatively high stiffness in a certain direction. Therefore, using CM as the backbone of the joint can improve the load-carrying capacity and motion precision. The PneuNets bending actuator shown in Fig. 1 consists of bellow-shape soft air chambers and an inextensible layer [23]. Pressuring the air chamber can inflate the lateral wall to contact the adjacent walls and generate moment. The moment will bend the actuator over a wide range. Compared with other bending actuators, the PneuNets bending actuator performs a high actuation rate, an extensive motion range, and a simple pressure–displacement relationship [24]. Those merits make it a good choice for joint actuation.

This paper proposes a new compliant hinge joint combining a compliant cross-axis flexural pivot with the PneuNets bending actuators. This joint can be in an active mode when pressurizing the

[1]Corresponding author.
Manuscript received July 2, 2023; final manuscript received December 12, 2023; published online January 12, 2024. Assoc. Editor: Guangbo Hao.

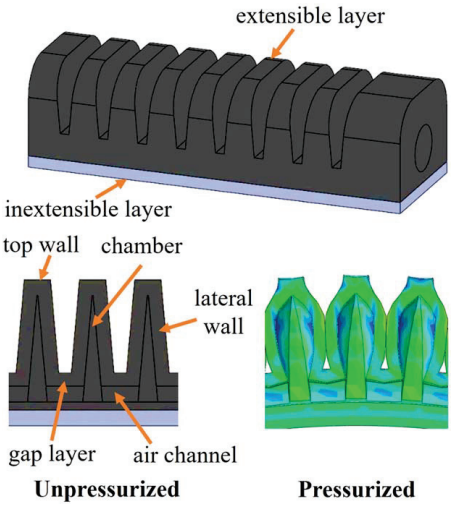

Fig. 1 Schematic of the PneuNets bending actuator

PneuNets bending actuator or in a passive mode driven by external force/moment. We derive a pseudo-rigid-body (PRB) model to study the pressure–displacement relationship in active mode and validate the result with experiments and simulations. Experiments are implemented to evaluate the motion in both active and passive modes. Also, we experimentally measure the in-axis and off-axis stiffnesses of the joint and calculate the stiffness ratio.

The paper is organized as follows: Sec. 2 presents the design of the new joint. We derive the analytical models for the PneuNets bending actuator and the joint in active mode. Then, in Sec. 3, we detail the fabrication process, the experiments for the joint's trajectory in both active and passive modes, and the experiments for the pressure–displacement relationship. We also develop finite element simulations to validate the theoretical model. A new design with higher motion precision is proposed based on the motion results. We also experimentally study the in-axis and off-axis stiffnesses and calculate the stiffness ratio. Finally, in Sec. 4, we conclude the paper.

2 Methods

In this section, we first detail the design. Then, we derive the theoretical model for the PneuNets bending actuator's driving moment and a compliant four-bar mechanism based on the PRB model for the kinematics and statics. We finally derive the pressure–displacement model by combining the PRB and driving moment models.

2.1 Joint Design. The proposed novel joint is called PneuNets actuated cross-axis flexural pivot (PnACF pivot). Figure 2 shows its computer-aided design (CAD) model and prototype. A compliant cross-axis flexural pivot made of relatively stiff material is used as the backbone, and two soft PneuNets bending actuators are bonded on the two flexure strips for actuation. As the two actuators are attached to the strips, pressurizing one of them will bend the strip and rotate the PnACF pivot around the *Z*-axis clockwise or counterclockwise. The strip also works as the inextensible layer to limit the unnecessary expansion of the actuator's bottom layer. Due to the high off-axis stiffness of the cross-axis flexural pivot, the PnACF pivot can carry a high payload in a non-motion direction while maintaining flexibility in the motion direction. Moreover, this high off-axis stiffness reduces the PnACF pivot's parasitic motion error.

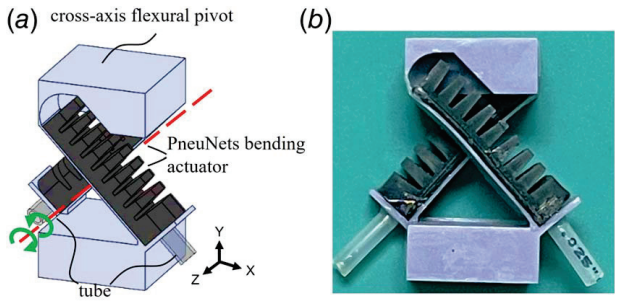

Fig. 2 Design of PneuNets actuated cross-axis flexural pivot: (*a*) CAD model and (*b*) prototype

2.2 Analytical Model of Driving Moment From the PneuNets Bending Actuator. The geometry of the PneuNets bending actuator is shown in Fig. 3(*a*). We assume the lateral wall of the chamber is the four-edges clamped thin walls under applied pressure, see Fig. 3(*b*). Under this assumption, the bulge height h of one chamber's lateral wall can be obtained by Srivastava and Hui [25]

$$h = \frac{a-s}{2\cos\theta_c}\tan\left(\frac{\theta_m}{2}\right) \tag{1}$$

where a is the chamber's inner height, s is the height of the gap layer, and θ_c is the angle of the tilt chamber. θ_m is the clamped angle of the lateral wall [25], which is determined by the following formula:

$$\theta_m = \frac{aP}{2\mu h_0}\cos\theta_c \tag{2}$$

where P is the air pressure, μ is the shear modulus, and h_0 is the lateral wall thickness. To simplify the problem, we assume that the elongation of the gap layer causes the bending of the PneuNets bending actuator. Therefore, the displacement h_1 of the lateral chamber wall at the gap layer, as shown in Fig. 3(*c*), can be calculated by the geometry relationship [26]

$$h_1 = \frac{2s}{a+s}h\cos\theta_c \tag{3}$$

From the geometric relationship, the total bending angle can be obtained

$$\theta = \frac{2(n-1)}{t_b+s}h_1, \tag{4}$$

where t_b is the thickness of the bottom layer of the PneuNets bending actuator.

The driving moment of the PneuNets bending actuator is composed of two components: the moment M_l generated by the lateral wall's inflation and contact, and the resistance moment M_r generated by the bending of the junction zone [9]. To determine

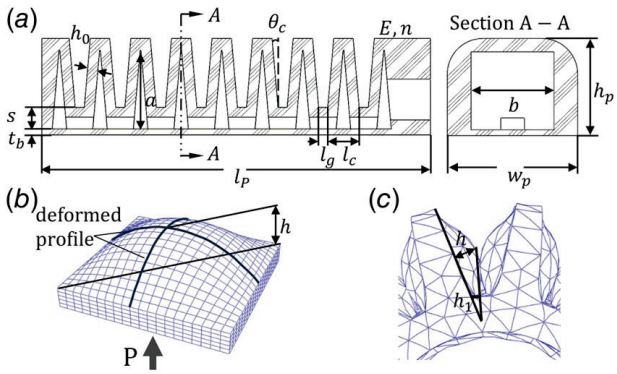

Fig. 3 (*a*) The geometry of the PneuNets bending actuator, (*b*) FEA of inflating lateral wall, and (*c*) FEA of two inflating chambers

the moment M_l, we selected a fourth-order polynomial function $f(\tau) = 0.46\tau^4 - 1.46\tau^2 + 1$ as the lateral wall's profile function, which satisfies the boundary condition and fits the actual profile well. The displacement field of the lateral wall is written as

$$\mathbf{u} = \left[0,\ 0,\ hf\left(\frac{2x}{b}\right)f\left(\frac{2\cos\theta_c y}{a}\right)\right]^T \tag{5}$$

where b is the inner width of the chamber. $\mathbf{x} = (x, y, z)^T$ are the coordinates of the lateral wall. Based on the profile function and Neo–Hookean model, the strain energy U_w and volume V of one deformed lateral wall can be obtained

$$U_w(h) = \int_{\frac{-h_0}{2}}^{\frac{h_0}{2}}\int_{\frac{-a}{2\cos\theta_c}}^{\frac{a}{2\cos\theta_c}}\int_{\frac{-b}{2}}^{\frac{b}{2}} C_1(I_1 - 3)\,\mathrm{d}x\,\mathrm{d}y\,\mathrm{d}z \tag{6}$$

$$V(h) = \int_{\frac{-h_0}{2}}^{\frac{h_0}{2}}\int_{\frac{-a}{2\cos\theta_c}}^{\frac{a}{2\cos\theta_c}}\int_{\frac{-b}{2}}^{\frac{b}{2}} f\left(\frac{2x}{b}\right)f\left(\frac{2\cos\theta_c y}{a}\right)\mathrm{d}x\,\mathrm{d}y\,\mathrm{d}z \tag{7}$$

where $I_1 = tr([(\mathbf{I} + \frac{\partial \mathbf{u}}{\partial \mathbf{x}})(\mathbf{I} + \frac{\partial \mathbf{u}}{\partial \mathbf{x}})^{\mathbf{T}}])$ is the first invariant. Here function $tr()$ represents the trace of a matrix. C_1 is the coefficient of the Neo–Hookean model. According to the principle of virtual work, we can obtain the following formula:

$$\frac{\mathrm{d}U_w(h)}{\mathrm{d}h}\frac{\mathrm{d}h}{\mathrm{d}\theta}\delta\theta = P\frac{\mathrm{d}V(h)}{\mathrm{d}h}\frac{\mathrm{d}h}{\mathrm{d}\theta}\delta\theta - M_l\delta\theta \tag{8}$$

Substituting Eqs. (4), (6), and (7) into Eq. (8), we can calculate the moment M_l generated by the deformation of one lateral wall. To calculate the resistance moment, we assume the undeformed junction zone on the bottom layer has a rectangular shape with the size of $(b/2) \times t_b \times (l_g/2)$, in which l_g is the length of the gap. After bending, the junction zone will deform into a sector with a central angle θ. We can obtain the resistance moment for the half-gap as follows:

$$M_r = b\int_0^{t_b}\left(\frac{\partial W}{\partial \lambda}\right)y\,\mathrm{d}y \tag{9}$$

where $\lambda = 1 + 2\theta y/(kl_g)$ is the stretch ratio, k is a factor larger than 1, and W is the strain energy density of the junction zone.

Combining Eqs. (8) and (9), the total driving moment is

$$M_d = 2(n-1)(M_l - M_r) \tag{10}$$

2.3 Pseudo-Rigid-Body Model of the PnACF Pivot for Kinematic and Static Analysis. We use a compliant four-bar mechanism based on the pseudo-rigid-body model [27] to analyze the kinematics of the PnACF pivot in active mode, as shown in Fig. 4(*a*). In this model, two pin joints connect the moving stage and the two strips, and two more pin joints are at the strip with a distance of γl, where γ is the characteristic factor, l is the length of the strip. Torsional springs with stiffness K are placed at each pin joint. In this way, rigid-body kinematics is sufficient to determine the PnACF pivot's motion. The link lengths of the PRB model are

$$\begin{aligned} r_1 &= (2\gamma - 1)w_h \\ r_2 &= r_4 = \gamma l \\ r_3 &= w_h \end{aligned} \tag{11}$$

where w_h is the width of the compliant cross-axis flexural pivot.

The following loop closure equations govern the kinematics of the four-bar mechanism:

$$r_2\cos\theta_2 + r_3\cos\theta_3 = r_1\cos\theta_1 + r_4\cos\theta_4 \tag{12}$$

$$r_2\sin\theta_2 + r_3\sin\theta_3 = r_1\sin\theta_1 + r_4\sin\theta_4 \tag{13}$$

As shown in Fig. 4(*b*), the PneuNets bending actuators are attached to two strips. Since the actuator's gap is much easier to bend than

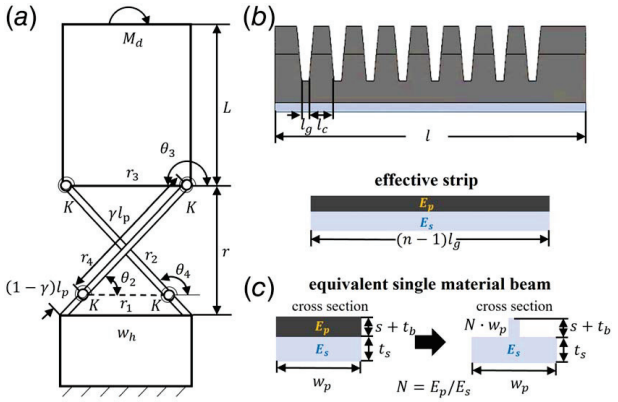

Fig. 4 (*a*) The PRB model of the PnACF pivot, (*b*) each strip is made of a PneuNet actuator bond to a flexure beam, and (*c*) the strip is modeled as a single material beam with equivalent bending stiffness

the part with the chamber, one strip with PneuNets bending actuator can be simplified into a uniform beam with the length $(n-1)l_g$, and the top layer's thickness is $s + t_b$. In this simplification, the effective strip is treated as a two-material composite beam with a rectangular cross section, for which Young's modulus of the top layer and the bottom layer are E_p and E_s, respectively. We can convert the composite beam into a single material beam by the equivalent area method as shown in Fig. 4(*c*) and calculate its effective moment of inertia I^*. So, the stiffness of the torsional spring is obtained by the following formula:

$$K = \gamma K_\Theta \frac{E_s I^*}{2(n-1)l_g} \tag{14}$$

where K_Θ is the stiffness coefficient. Both two coefficients γ and K_Θ can be determined by the optimization method, which minimizes the error compared to the finite element analysis (FEA) results. After knowing the coefficients, we can obtain the moment–deflection characteristic of the PnACF pivot by the principle of virtual work, which is expressed as

$$M_d = T_2 + T_3 - (T_1 + T_2)\frac{r_3\sin(\theta_3 - \theta_4)}{r_2\sin(\theta_4 - \theta_2)} - (T_3 + T_4)\frac{r_3\sin(\theta_3 - \theta_2)}{r_4\sin(\theta_4 - \theta_2)} \tag{15}$$

where

$$\begin{aligned} T_1 &= K(\theta_2 - \theta_{20}) \\ T_2 &= K(\theta_2 - \theta_{20} - \theta_3 + \theta_{30}) \\ T_3 &= K(\theta_4 - \theta_{40} - \theta_3 + \theta_{30}) \\ T_4 &= K(\theta_4 - \theta_{40}) \end{aligned} \tag{16}$$

The subscript "0" represents undeflected angles. Combining Eq. (10) in Sec. 2.2 with Eq. (15), we can establish the relationship between pressure and the rotational angle of the PnACF pivot.

3 Results

After finalizing the design and modeling of the PnACF pivot, we manufacture a prototype and evaluate its performance through experiments and simulations. We first fabricate a prototype by resin printing. The geometric parameters of the actuator and the cross-axis flexural pivot are shown in Tables 1 and 2, respectively. Then, we evaluate the motion of the PnACF pivot in both active and passive modes. Based on the results, we propose a new design with different parameters to improve motion performance in passive

Table 1 Parameters of the PneuNets bending actuator

Parameter	s (mm)	n	t_b (mm)	h_0 (mm)	a (mm)	b (mm)
Value	1.83	9	0.5	0.88	6.69	7

Parameter	θ_c (rad)	l (mm)	l_g (mm)	l_c (mm)	w_p (mm)	h_p (mm)
Value	0.09	33.98	0.78	2.5	11	8.72

Table 2 Parameters of the cross-axis flexural pivot (unit: mm)

Parameter	w_h	r	l	L	t_s
Value	24	24	33.98	10	0.5

mode. Finally, we conduct experiments to study the in-axis and off-axis stiffnesses of both two designs.

3.1 Material Selection and Fabrication. Due to the complex shape of the PneuNets bending actuator and multi-material manufacturing requirements, the traditional casting method is not suitable for this project. Instead, this work uses the resin printing method to fabricate the actuator and the cross-axis flexural pivot with a DLP printer (AnyCubic Inc., Shenzhen, China). We first print two actuators using a commercial rubber-like resin (F69, Resione Inc., Dongguan City, China) and post-process them for 10 min with a curing machine (AnyCubic Inc.). Then, we print the cross-axis flexural pivot with a flexible and tough resin (UV Tough resin, AnyCubic Inc., Shenzhen, China) and do the post-processing for 3 min. Finally, we bond two actuators on the two strips of the pivot by super glue. We glue the actuator's bottom to the strip's top. A tensile test is implemented to determine the material properties of the rubber-like resin following the standard ASTM-D412 type C. Five dumbbell specimens are fabricated and stretched until they break on the tensile machine (Instron5542). The strain rate is 500 mm/min. The Neo–Hookean model is used to fit the testing data, and the mean value of Young's Modulus from testing is 3.93 MPa. This value is used in FE simulations and analytical solutions.

3.2 Finite Element Simulations. A finite element model is built in ABAQUS. Young's modulus of the cross-axis flexural pivot is set to 1 GPa, and Poisson's ratio of the pivot is 0.35. Based on the tensile testing, we use the Neo–Hookean model with coefficients $C_1 = 0.66$ and $D_1 = 0$ as the constitutive model of the PneuNets bending actuator. Pressure up to 0.276 MPa (40 psi) is applied on the internal surfaces of chambers of one actuator for the PnACF pivot's unidirectional rotation. The fixed stage of the pivot and the end of two actuators close to the fixed stage are fixed. Self-contact interaction is defined between adjacent chamber walls. The hybrid tetrahedron element C3D10H is assigned to the actuator, and the element C3D10 is used for the cross-axis flexural pivot.

3.3 Experiments for Motion Evaluation. The PnACF pivot has active and passive modes. In active mode, the PnACF pivot works as an active joint, meaning that the PneuNets bending actuator will drive the joint with air pressure. In passive mode, the PnACF pivot works as a passive joint, meaning that the external force will move the joint but not the actuator. Before the experiment starts, we define three translational directions (X, Y, Z) along the X-, Y-, and Z-axis and three rotational directions (RX, RY, RZ) around the X-, Y-, and Z-axis. The deformation axes are shown in Fig. 5(*a*). The experiment setup for the active mode is shown in Fig. 5(*b*). In which the PnACF pivot with an indicator is fixed on the table, and a camera is placed above it. One of the actuators is gradually pressurized from 0 MPa (0 psi) to 0.276 MPa (40 psi) to drive the pivot rotation. The camera captures the rotation angle corresponding to each pressure. Then, the IMAGEJ software is used to measure the angle in the pictures. To measure the angle, we draw the initial position of the indicator tip and rotation center on the grip paper. Then, we connect those two points and the center and current position of the tip in the picture. The angle can be automatically calculated by the tool in the software. We repeated the experiment thrice for each direction and calculated the average. Figure 5(*c*) shows the experiment setup for passive mode. The moving stage of the pivot is tied to the Mark 10 force sensor by a thin wire. The force sensor will move and rotate the pivot by turning the knob. The sensor records the driving forces, and the angle corresponding to each driving force is recorded by the camera above the pivot.

Our first design (Design 1) is pivot with the cross center in the strip's middle. We define the length ratio from the moving stage to the center over the total length of the strip as a_l. Thus, for Design 1, $a_l = 0.5$. As shown in Fig. 6(*a*), given the dimensions in Tables 1 and 2, the ideal motion trajectory of the center point on the moving stage is a semi-circle with a radius of 22 mm relative to the cross center. We plot the trajectories in active and passive modes from the experiments in Figs. 6(*b*) and 6(*c*). We also calculate the absolute error of radius referring to the ideal trajectory for both modes and compared them in Fig. 6(*d*). From the result, the mean error in the passive mode is 0.1150, and that for the active

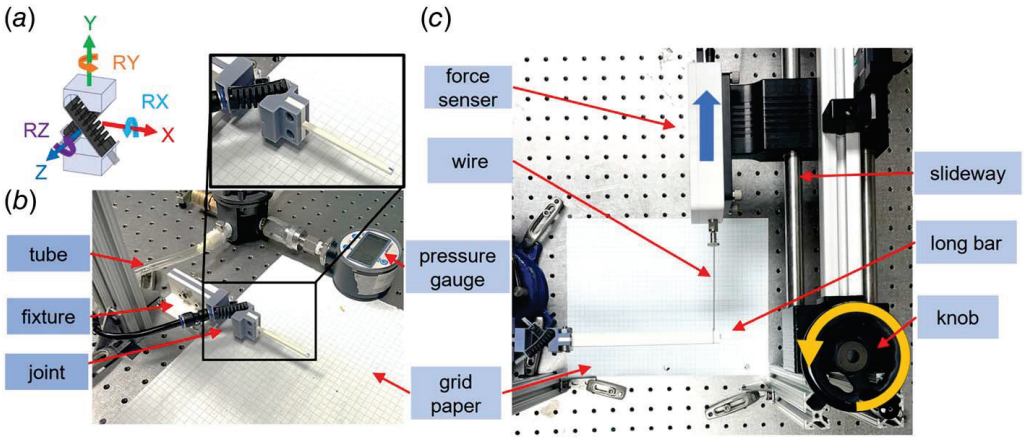

Fig. 5 Experiments of the PnACF pivot: (*a*) deformation axes, (*b*) experiment setup for the active mode, and (*c*) experiment setup for the passive mode

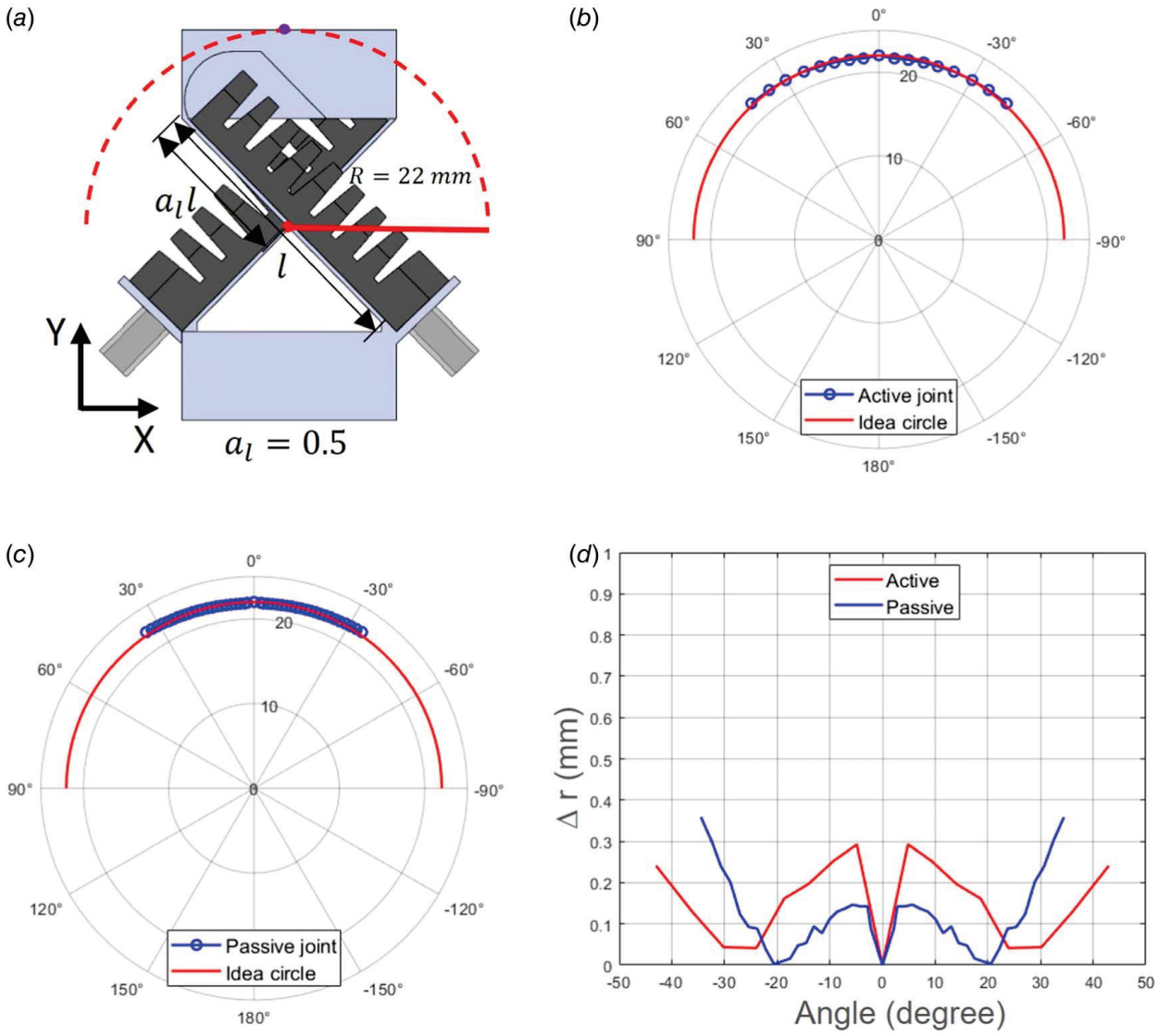

Fig. 6 Deformation of Design 1 with $a_l = 0.5$: (*a*) schematic view, (*b*) trajectory of Design 1 in the active mode, (c) trajectory of Design 1 in the passive mode, and (*d*) motion error of both modes

mode is 0.1397. The main reason for the error is that the center axis of Design 1 will drift along the *X* and *Y* directions when rotating.

We compare the pressure–angle curve in the active mode from the analytical model with the curve from the experiment and FE simulation in Fig. 7. From the result, the error of the analytical model compared to the simulation is 1.15%, and it is 4.47% compared to the experiment. The reason is that the small amount of residual resin in the air chamber blocks the deformation of the actuator. Therefore, the PnACF pivot in the experiment cannot achieve as large as an angle in the simulation at the maximum air pressure. Within the pressure range of [0 MPa, 0.276 MPa], the analytical model and FEA show that the pivot can rotate in a range of [−43 deg, 43 deg]. And the experiment result shows a range of [−38 deg, 39 deg]. The result also shows a close to linear relationship, which means the PnACF pivot can be easily controlled to achieve a specific angle by air pressure.

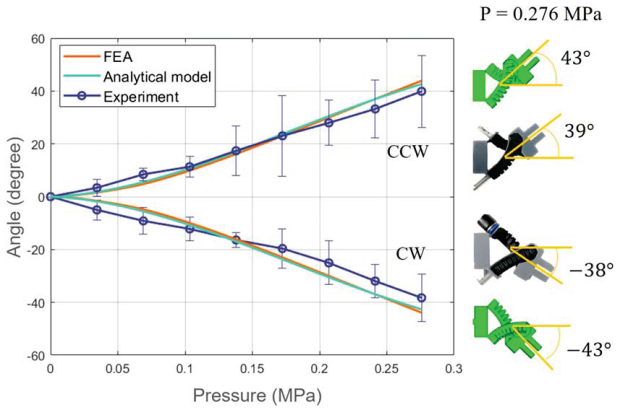

Fig. 7 Comparison of pressure–angle curves from FE simulation, analytical model, and experimental testing

3.4 An Improved Design With Smaller Motion Error. To improve the PnACF pivot's performance in the passive mode, we propose a new design (Design 2) with $a_l = 0.5 + \sqrt{(5)}/6$ as shown in Fig. 8(*a*). The other geometric parameters are consistent with Design 1, except that the number of chambers *n* is reduced to 7. Based on Ref. [28], the center axis of Design 2 has zero error along the *Y*-axis and little error along the *X*-axis when rotating. The experiment results of trajectory in both active and passive modes are shown in Figs. 8(*b*) and 8(*c*), and errors are compared in Fig. 8(*d*). It shows that the mean error of Design 2 in

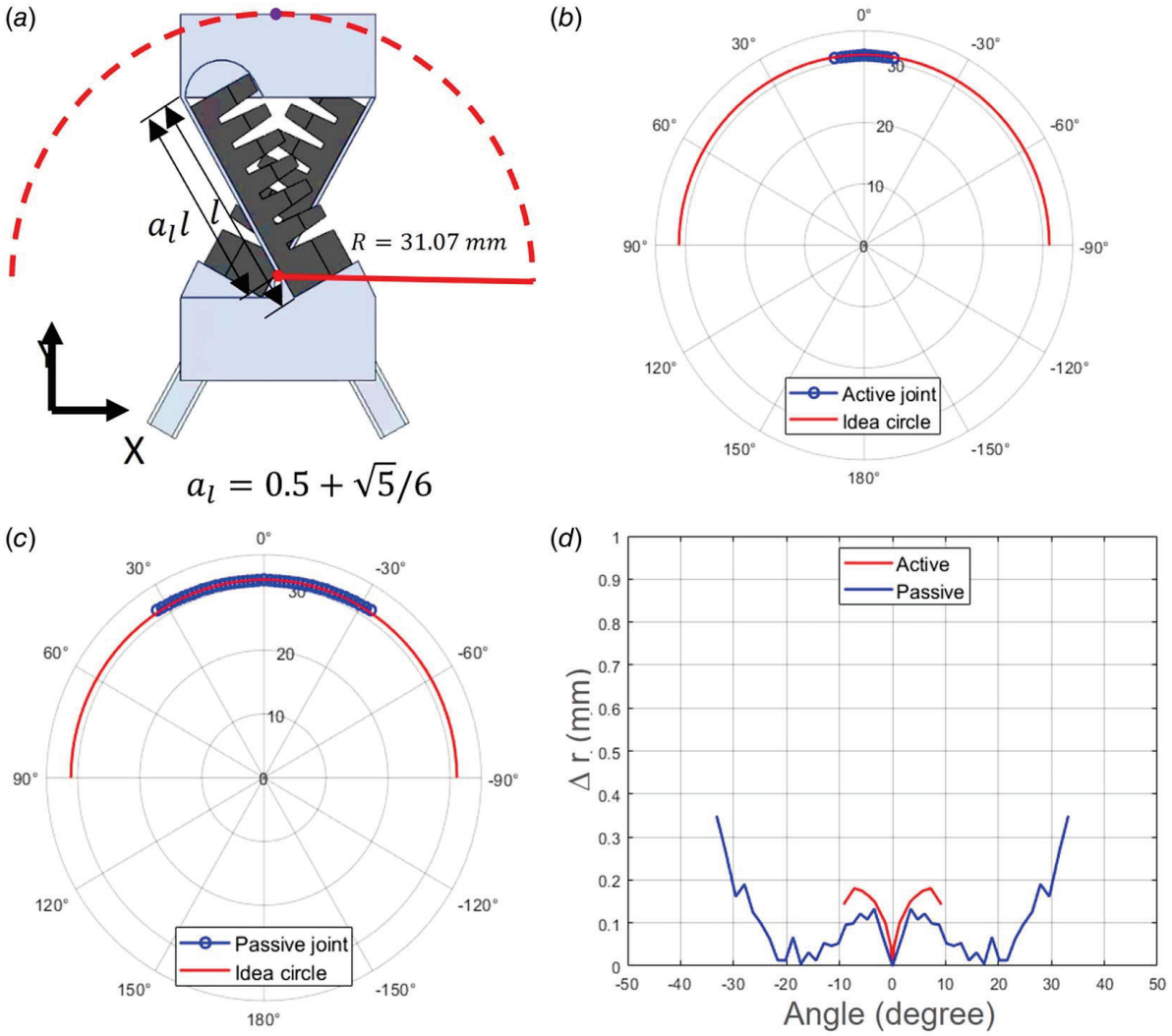

Fig. 8 Deformation of Design 2 with $a_l = 0.5 + \sqrt{(5)}/6$: (*a*) schematic view, (*b*) trajectory of Design 2 in the active mode, (*c*) trajectory of Design 2 in the passive mode, and (*d*) motion error of both modes

passive mode is 0.0946, less than that of Design 1. The error in the active mode is 0.1161, which is also less than that of Design 1. However, the rotational stiffness of Design 2 is higher, so in the active mode, Design 2 can only achieve 9.2 deg at 0.276 MPa.

3.5 Experiments for Stiffness Evaluation. We conducted four experiments to measure each design's in-axis stiffness (*RZ* direction) and three off-axis stiffness (*RX*, *Y*, and *Z* direction).

Figures 9(*a*) and 9(*b*) show the experimental setup for measuring the rotational stiffness. We used a wire to connect the Mark 10 force sensor and the pivot's moving stage. The length r_c between the connecting point and the cross center for Design 1 and Design 2 are 37 mm and 46.07 mm, respectively. By turning the knob clockwise, the force sensor can move away from the pivot and drive it to rotate. The force F can be read from the sensor, and the moment can be calculated by $M = F \times r_c$. The camera above the pivot records the angle, which is measured by the IMAGEJ.

Figures 9(*c*) and 9(*d*) illustrate the experimental setup for measuring translational stiffness. When turning the knob counterclockwise, the tip of the force sensor will push the pivot to move along the direction to be measured. The traveling sensor and force sensor, respectively, can record the displacement and force data.

Figures 10(*a*) and 10(*b*) show the moment–angle curve and force–displacement curve of Design 1, and the results of Design 2

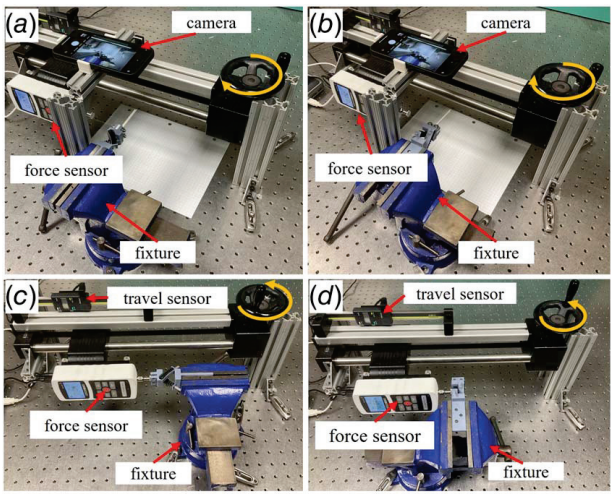

Fig. 9 Stiffness experiments setup: (*a*) *RZ* direction, (*b*) *RX* direction, (*c*) *Y* direction, and (*d*) *Z* direction

are shown in Figs. 10(*c*) and 10(*d*). We calculate each design's rotational and translational stiffness based on those data. To compare a rotational stiffness with a translational stiffness, we

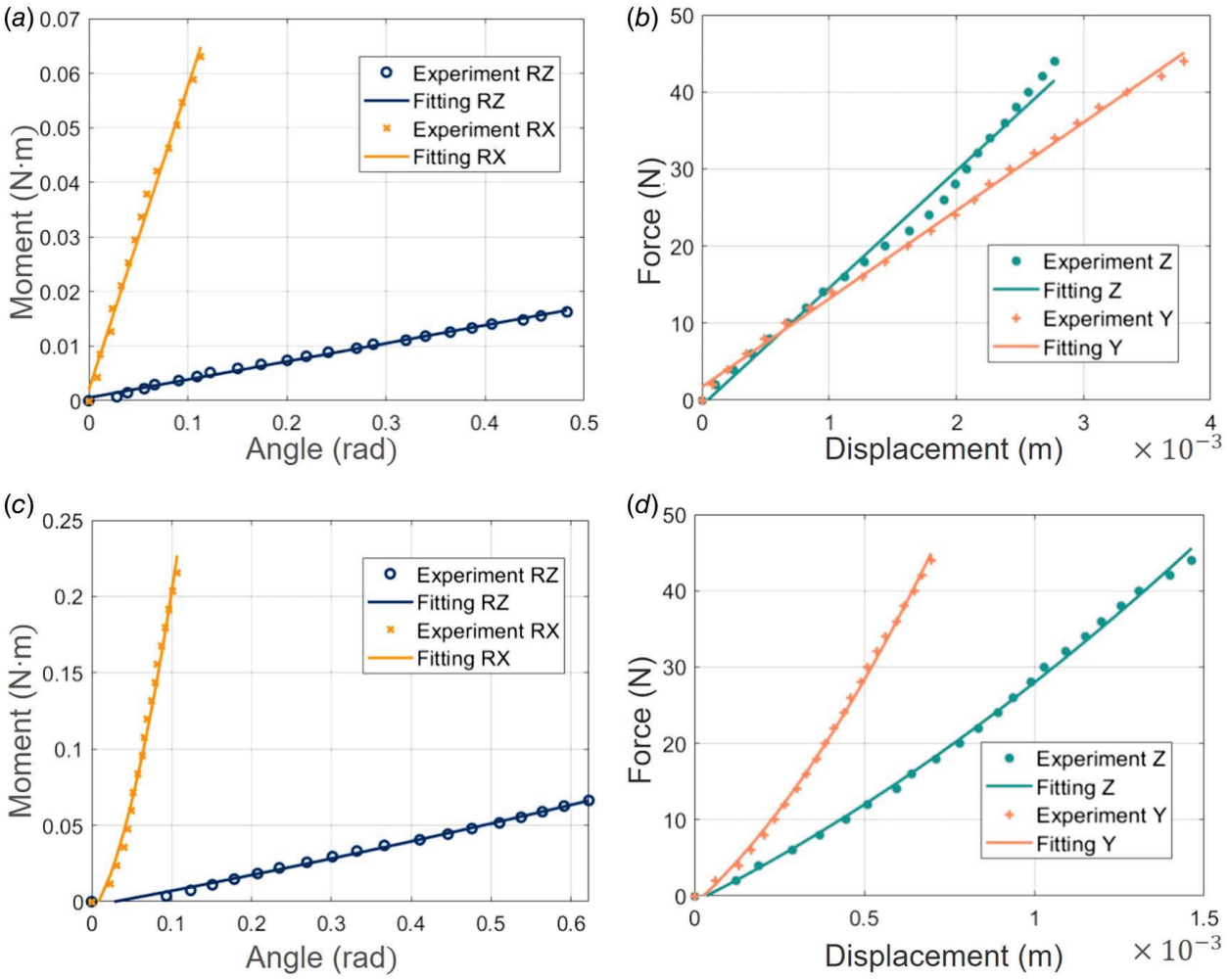

Fig. 10 Stiffness experiments results: (*a*) moment–angle curve of Design 1, (*b*) force–displacement curve of Design 1, (*c*) moment–angle curve of Design 2, and (*d*) force–displacement curve of Design 2

Table 3 Stiffness and stiffness ratio of Design 1

	$K_{\theta Z}$	$K_{\theta X}$	K_Y	K_Z
Stiffness (N/m)	24.25	405.92	1.144e4	1.522e4
Stiffness ratio	1	16.74	471.75	627.63

Table 4 Stiffness and stiffness ratio of Design 2

	$K_{\theta Z}$	$K_{\theta X}$	K_Y	K_Z
Stiffness (N/m)	45.51	426.41	4.052e4	2.184e4
Stiffness ratio	1	9.37	890.30	479.97

convert rotational stiffness K_r to its' equivalent translation stiffness by dividing the square of a nominal length r_t [29]. In other words, the equivalent translational stiffness of $K_{\theta Z}$, $K_{\theta Z}$ can be calculated as

$$K_{\theta Z} = \frac{K_{rz}}{(r_t)^2}, \quad K_{\theta X} = \frac{K_{rx}}{(r_t)^2} \tag{17}$$

where K_{rz} and K_{rz} are the rotational stiffness along *RZ* and *RX* directions, respectively. $r_t = 37$ mm for Design 1 and $r_t = 46.07$ mm for Design 2 are the length from the force point to the cross center.

Based on the equivalent translational stiffness, we can calculate the stiffness ratio, defined as the ratio of off-axis stiffness and in-axis stiffness. The results are listed in Tables 3 and 4. For Design 1, the stiffness in the *RX* direction is 16.74 times the stiffness in the *RZ* direction, and the stiffness in the *Y* and *Z* directions is 471.75 times and 627.63 times the stiffness in the *RZ* direction, respectively. For Design 2, the stiffness in the *RX* direction is 9.37 times the stiffness in the *RZ* direction, and the stiffness in the *Y* and *Z* directions is 890.30 times and 479.97 times the stiffness in the *RZ* direction, respectively. A high stiffness ratio means the PnACF pivot has a large load-carry capacity off-axis while maintaining the compliance in-axis.

4 Conclusions

In this paper, we present the design and analysis of a PneuNets actuated cross-axis flexural pivot. Experiments and FEA simulations are developed to evaluate the motion of the proposed design in active and passive modes. The results show that the design has a relatively large motion range, and the pressure–displacement curve is close to linear. However, the motion error of this design is large in both passive and active modes. To address this shortcoming, we proposed an improved design that has a relatively small motion error at the cost of the limited motion range in the active mode due to high rotational stiffness. Experimental testings show that the two designs have a high stiffness ratio of off-axis to in-axis, which means they can carry heavy loads in the off-axis

directions. Our design can be essential to soft robots with enhanced payload capacity and precise motion.

Acknowledgment

This material is based upon work supported by the National Science Foundation under Grant No. 2019648. Any opinions, findings, and conclusions or recommendations expressed in this material are those of the author(s) and do not necessarily reflect the views of the funding agencies.

Conflict of Interest

There are no conflicts of interest.

Data Availability Statement

The datasets generated and supporting the findings of this article are obtainable from the corresponding author upon reasonable request.

References

[1] El-Atab, N., Mishra, R. B., Al-Modaf, F., Joharji, L., Alsharif, A. A., Alamoudi, H., Diaz, M., Qaiser, N., and Hussain, M. M., 2020, "Soft Actuators for Soft Robotic Applications: A Review," Adv. Intell. Syst., **2**(10), p. 2000128.
[2] Schiller, L., Seibel, A., and Schlattmann, J., 2019, "Toward a Gecko-Inspired, Climbing Soft Robot," Front. Neurorobot., **13**, p. 106.
[3] Singh, G., Patiballa, S., Zhang, X., and Krishnan, G., 2019, "A Pipe-Climbing Soft Robot," 2019 International Conference on Robotics and Automation (ICRA), Montreal, Canada, May 20–24, pp. 8450–8456.
[4] Drotman, D., Jadhav, S., Karimi, M., de Zonia, P., and Tolley, M. T., 2017, "3D Printed Soft Actuators for a Legged Robot Capable of Navigating Unstructured Terrain," 2017 IEEE International Conference on Robotics and Automation (ICRA), Marina Bay Sands, Singapore, May 29–June 3, pp. 5532–5538.
[5] Ishida, M., Drotman, D., Shih, B., Hermes, M., Luhar, M., and Tolley, M. T., 2019, "Morphing Structure for Changing Hydrodynamic Characteristics of a Soft Underwater Walking Robot," IEEE Rob. Autom. Lett., **4**(4), pp. 4163–4169.
[6] Cheng, P., Ye, Y., Yan, B., Lu, Y., and Wu, C., 2022, "Eccentric High-Force Soft Pneumatic Bending Actuator for Finger-Type Soft Grippers," ASME J. Mech. Rob., **14**(6), p. 060908.
[7] Crowley, G. B., Zeng, X., and Su, H. -J., 2022, "A 3D Printed Soft Robotic Gripper With a Variable Stiffness Enabled by a Novel Positive Pressure Layer Jamming Technology," IEEE Rob. Autom. Lett., **7**(2), pp. 5477–5482.
[8] Wang, J., Liu, Z., and Fei, Y., 2018, "Design and Testing of a Soft Rehabilitation Glove Integrating Finger and Wrist Function," ASME J. Mech. Rob., **11**(1), p. 011015.
[9] Wang, J., Fei, Y., and Pang, W., 2019, "Design, Modeling, and Testing of a Soft Pneumatic Glove With Segmented PneuNets Bending Actuators," IEEE/ASME Trans. Mechatron., **24**(3), pp. 990–1001.
[10] Wang, N., Chen, B., Ge, X., Zhang, X., and Chen, W., 2021, "Design, Kinematics, and Application of Axially and Radially Expandable Modular Soft Pneumatic Actuators," ASME J. Mech. Rob., **13**(2), p. 021019.
[11] Zhang, Y., Li, P., Quan, J., Li, L., Zhang, G., and Zhou, D., 2023, "Progress, Challenges, and Prospects of Soft Robotics for Space Applications," Adv. Intell. Syst., **5**(3), p. 2200071.
[12] Cianchetti, M., Laschi, C., Menciassi, A., and Dario, P., 2018, "Biomedical Applications of Soft Robotics," Nat. Rev. Mater., **3**(6), pp. 143–153.
[13] Liu, J., Wei, J., Zhang, G., Wang, S., and Zuo, S., 2019, "Pneumatic Soft Arm Based on Spiral Balloon Weaving and Shape Memory Polymer Backbone," ASME J. Mech. Des., **141**(8), p. 082302.
[14] Zeng, X., Hurd, C., Su, H.-J., Song, S., and Wang, J., 2020, "A Parallel-Guided Compliant Mechanism With Variable Stiffness Based on Layer Jamming," Mech. Mach. Theory, **148**, p. 103791.
[15] Su, H., Hou, X., Zhang, X., Qi, W., Cai, S., Xiong, X., and Guo, J., 2022, "Pneumatic Soft Robots: Challenges and Benefits," Actuators, **11**(3), p. 92.
[16] Kim, Y.-J., Cheng, S., Kim, S., and Iagnemma, K., 2013, "A Novel Layer Jamming Mechanism With Tunable Stiffness Capability for Minimally Invasive Surgery," IEEE Trans. Rob., **29**(4), pp. 1031–1042.
[17] Alambeigi, F., Seifabadi, R., and Armand, M., 2016, "A Continuum Manipulator With Phase Changing Alloy," 2016 IEEE International Conference on Robotics and Automation (ICRA), Stockholm, Sweden, May 16–21, pp. 758–764.
[18] Yang, Y., Chen, Y., Li, Y., Chen, M. Z., and Wei, Y., 2017, "Bioinspired Robotic Fingers Based on Pneumatic Actuator and 3D Printing of Smart Material," Soft Rob., **4**(2), pp. 147–162.
[19] Liu, M., Hao, L., Zhang, W., and Zhao, Z., 2020, "A Novel Design of Shape-Memory Alloy-Based Soft Robotic Gripper With Variable Stiffness," Int. J. Adv. Rob. Syst., **17**(1), p. 1729881420907813.
[20] Ozkan-Aydin, Y., Chong, B., Aydin, E., and Goldman, D. I., 2020, "A Systematic Approach to Creating Terrain-Capable Hybrid Soft/Hard Myriapod Robots," 2020 3rd IEEE International Conference on Soft Robotics (RoboSoft), New Haven, CT, May 15–July 15, pp. 156–163.
[21] Lotfiani, A., Zhao, H., Shao, Z., and Yi, X., 2019, "Torsional Stiffness Improvement of a Soft Pneumatic Finger Using Embedded Skeleton," ASME J. Mech. Rob., **12**(1), p. 011016.
[22] Howell, L. L., 2001, *Compliant Mechanisms*, John Wiley & Sons, Hoboken, NJ.
[23] Mosadegh, B., Polygerinos, P., Keplinger, C., Wennstedt, S., Shepherd, R. F., Gupta, U., Shim, J., Bertoldi, K., Walsh, C. J., and Whitesides, G. M., 2014, "Pneumatic Networks for Soft Robotics that Actuate Rapidly," Adv. Funct. Mater., **24**(15), pp. 2163–2170.
[24] Rus, D., and Tolley, M. T., 2015, "Design, Fabrication and Control of Soft Robots," Nature, **521**(7553), pp. 467–475.
[25] Srivastava, A., and Hui, C.-Y., 2013, "Large Deformation Contact Mechanics of Long Rectangular Membranes. I. Adhesionless Contact," Proc. R. Soc. A: Math., Phys. Eng. Sci., **469**(2160), p. 20130424.
[26] Liu, Z., Wang, F., Liu, S., Tian, Y., and Zhang, D., 2021, "Modeling and Analysis of Soft Pneumatic Network Bending Actuators," IEEE/ASME Trans. Mechatron., **26**(4), pp. 2195–2203.
[27] Jensen, B. D., and Howell, L. L., 2002, "The Modeling of Cross-axis Flexural Pivots," Mech. Mach. Theory., **37**(5), pp. 461–476.
[28] Hongzhe, Z., and Shusheng, B., 2010, "Accuracy Characteristics of the Generalized Cross-Spring Pivot," Mech. Mach. Theory, **45**(10), pp. 1434–1448.
[29] Zhang, Y., Su, H.-J., and Liao, Q., 2014, "Mobility Criteria of Compliant Mechanisms Based on Decomposition of Compliance Matrices," Mech. Mach. Theory, **79**, pp. 80–93.